I.   Transient Absorption Spectroscopy

Setup

The femtosecond laser setup used to record the transient absorption (TA) data was based on a Spitfire Pro XP amplifier seeded by a Mai Tai (both from Spectra-Physics). The central output wavelength was 795 nm with a 60 fs pulse length delivered at 1 kHz repetition frequency. The beam was split along two pathways; one pumping a collinear optical parametric amplifier (TOPAS-C, Light Conversion) to generate the pump beam. The other was led through a delay line and used to generate the white-light continuum probe using a 3 mm CaF_2 translating optical window. The probe pulse was split into two parts; the first directed towards the sample where it was overlapped with the collinear pump pulse, the other used as reference. The probe and reference beams were brought to the slit of a spectrograph and dispersed onto a double photodiode array, each with 512 elements (Pascher Instruments). The mutual polarization between pump and probe beams was set to 54.7° by placing Berek compensator in the pump beam.

Experimental Conditions

Samples consisted $[Fe(CN)_4(bpy)]^{2-}$ in dimethyl sulfoxide solution, measured in 1 mm quartz cuvettes and prepared at concentrations resulting in an OD of 0.3 at the pump wavelength of 650 nm. To determine the Group Velocity Dispersion (GVD) of the probe light, the cross-phase modulation signal was measured for the neat solvent of each sample under identical experimental conditions. The intensity of the pump pulse was kept below 10^{14} photons/cm²/pulse.

Data Treatment

Correction curves for the GVD were determined from the cross-phase modulation signal and used to correct time-zero for each recorded spectrum.

Global Analysis

The excited state kinetics were first investigated in a principal component analysis framework based on singular value decomposition of the datasets as described in Liu et al. [Liu]. Multi-exponential fitting

to the time-evolution of the singular vectors returned the characteristic timescale of the evolution of the transient data forming the base for the global analysis (GA).

The GA of $[Fe(CN)_4(bpy)]^{2-}$ yields two decay associated spectra (DAS) shown in Figure S1 D. Both DAS1 and DAS2 have distinct excited state absorption (ESA) features at 370 nm and a smaller feature at 540 nm. DAS1 describe a dampening and blue-shift of the 370 nm ESA and a red-shift of the 540 nm ESA happening with a time constant of 2.4 ps.

Fig. S1. [Fe(CN)$_4$(bpy)]$^{2-}$ in dimethyl sulfoxide two dimensional time-dependent UV visible absorption data (A) experimental difference spectra and (B) Global analysis fit. (C) Residuals and (D) the resulting decay associated spectra.
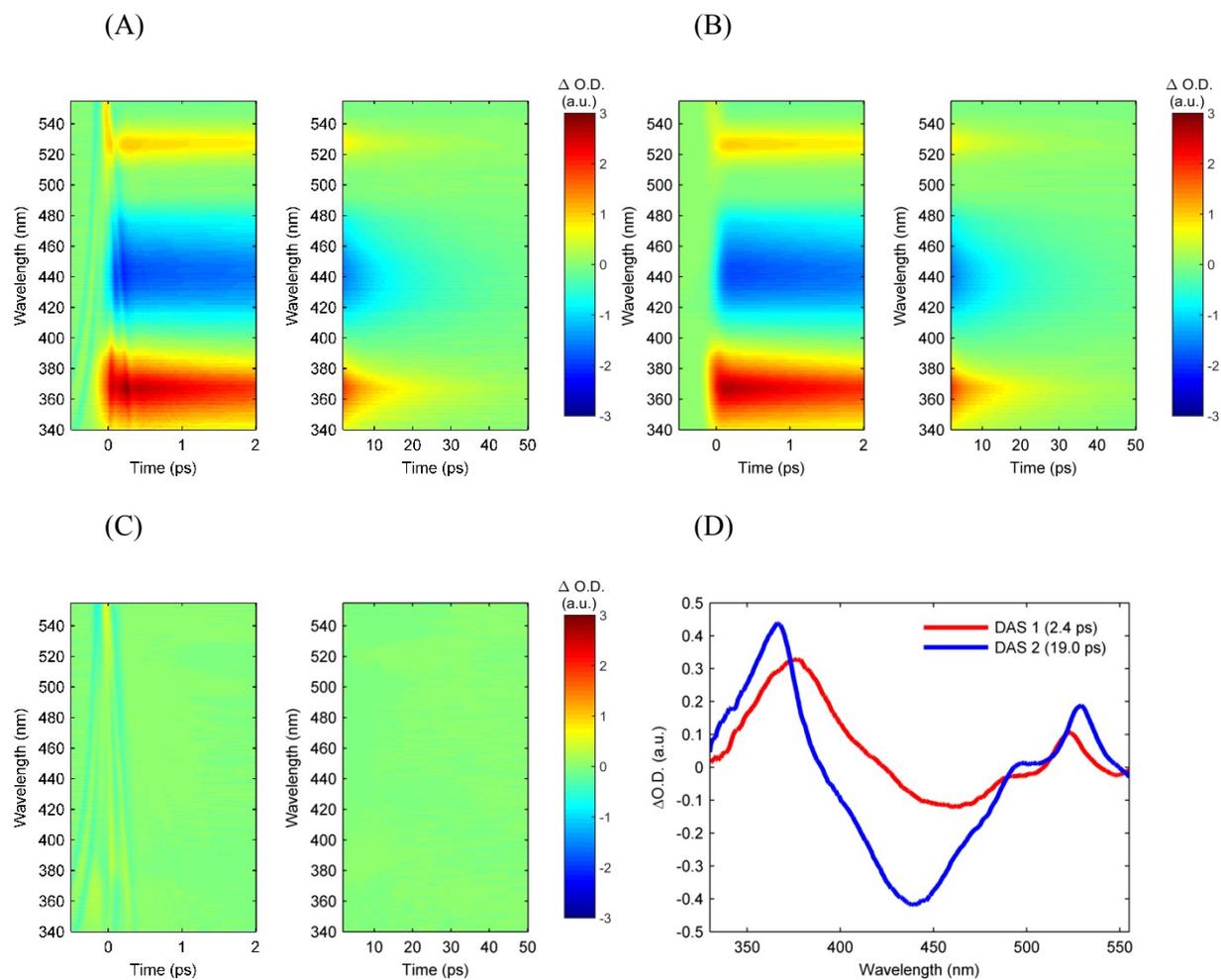
II.   X-ray Fluorescence Spectroscopy

Setup

The setup for X-ray Emission Spectroscopy at the X-ray Pump Probe (XPP) beamline at the Linear Coherent Light Source (LCLS) is similar to the one described in the Online Method section of Zhang et. al (REF Zhang). The experiment used a 0.1 mm thick planar liquid jet oriented at an angle of 45° with respect to the direction of the incident X-ray beam. The sample solution was collinearly excited with a 70 fs FWHM visible laser beam generated by optical parametric amplification of the 800 nm output of a Ti:sapphire regenerative amplifier laser system (Coherent, Legend). The 8 keV x-ray laser pulses, with an average bandwidth of 0.3%, were focused using Be compound refractive lenses to a 200 μm diameter spot size at the sample position.

The incoming x-ray pulse energy was measured using noninvasive diagnostics before the sample. A high-resolution energy dispersive x-ray emission spectrometer (REF Alonso-Mori 1), based on the von Hamos geometry, was used to capture the Fe 3p-1s (Kβ) fluorescence. The spectrometer was equipped with 4 cylindrically bent (500 mm radius) Ge(620) crystal analyzers and the central Bragg angle was set to 79.1 degrees. A CSPAD 2D pixel array detector (388x356 pixels) intersected x-rays diffracted from the crystal analyzers in the energy range from 7028-7084 eV (REF Koerner).

Data Treatment

The CSPAD detector recording the Kβ fluorescence was calibrated through a pixel dependent dark current (pedestal) subtraction, a common mode off-set subtraction, and an experimentally determined gain map. The gain map was built from histograms of each pixel response extracted from multiple images (after dark current and common mode subtraction) collected over many minutes. Gaussians were fit to the zero and one photon peaks of the histograms, enabling fine-tuned dark and gain corrections to the histograms directly from the data. The zero photon peaks were centered at zero analog-to-digital units and the separation between the zero and one photon peaks were scaled to unity for all pixels. The counts for each pixel in a given time-step were obtained by averaging the analog-to-digital values above a threshold

of 2.5σ of the zero-photon peak and scaling to the incident x-ray intensity. The final 1D spectrum for each time-step was obtained by integrating the signal in the nondispersive direction as described in (REF Alonso-Mori 2). The signal from the PIPS diode measuring the Kα fluorescence was scaled to the incoming intensity for each exposure, before integrating all exposures pertaining to same time-step.

The shot-to-shot x-ray-optical relative time of arrival fluctuations were measured for every x-ray-optical pulse pair with a timing diagnostic tool based on optical detection of x-ray generated carriers in a Si3N4 thin film (Harmand). This experimental measure of the relative timing was used to sort each experimental shot by the relative time of arrival. Thus, the final time resolution of the experiment results from the convolution of the optical and x-ray pulse durations, the difference group velocity of the x-ray and optical pulses in the sample, and the error in the relative time of arrival measurement. These set the resolution to roughly 150 fs FWHM.

Experimental Conditions

Samples consisted of 50 mM $[Fe(CN)_4(bpy)]^{2-}$ in dimethyl sulfoxide solution, resulting in an OD of 1 at the 650 nm pump wavelength. The intensity of the pump pulses were set to 4×10^{14} photon/cm^2/pulse to match the increased concentration compared to the TA measurements.

III.   Modeling the Transient X-ray Fluorescence Measurements

<u>Model Spectra</u>

We have constructed model spectra for the potential excited states of $[Fe(CN)_4(bpy)]^{2-}$ from ground-state iron complexes with different spin moments. Using ground state spectra to model the excited state spectra of distinct molecules have limitations that must be considered when choosing the model complexes. A variety of measurements and calculated spectra have demonstrated that the $K\beta$ spectrum shows little sensitivity to molecular symmetry for equal spin states, (Vanko 2006, Lee 2010) but the covalency of the metal-ligand bond does have an impact on the spectrum. (Pollock 2014) Since the $K\beta$ spectrum reflects the Fe contribution to the molecular spin moment, the impact of the metal-ligand bond covalency on the spectrum can be most clearly demonstrated for high spin ferric iron complexes at the extremes of metal-ligand covalency (Pollock 2014). For this reason we have constructed reference difference spectra from complexes with porphyrin, phthalocyanine, and cyanide ligands to ensure similar bonding characteristics to $[Fe(CN)_4(bpy)]^{2-}$ to use in the analysis. In previous analyses of $K\beta$ emission data [Zhang], the ground state and ^{1,3}MLCT spectra were modeled by the molecular system under investigation itself, and the oxidized compound respectively. It has not been possible to isolate the oxidized ground state compound; $[Fe(CN)_4(bpy)]^{-}$ under conditions that would make $K\beta$ reference measurements possible. Thus, to ensure accurate representation of both ground state and ^{1,3}MLCT spectra, we have recorded high resolution $K\beta$ fluorescence spectra of $[Fe(bpy)_3]^{2+}$, $[Fe(bpy)_3]^{3+}$, $[Fe(CN)_6]^{4-}$, and $[Fe(CN)_6]^{3-}$, and used these spectra to construct our reference spectra. The model spectrum of the ground state are modelled by the $[Fe(bpy)_3]^{2+}$ and $[Fe(CN)_6]^{4-}$ spectra, which are compared to the ground state $[Fe(CN)_4(bpy)]^{2-}$ spectrum recorded at the XFEL setup in Figure S2(A). While the ground state spectra of $[Fe(bpy)_3]^{2+}$ and $[Fe(CN)_6]^{4-}$ show considerable deviation around 7052 eV, a good representation of the $[Fe(CN)_4(bpy)]^{2-}$ spectrum is achieved by a linear combination of the two model spectra with a weight of 1/3 $[Fe(bpy)_3]^{2+}$ and 2/3 parts $[Fe(CN)_6]^{4-}$ consistent with the number of ligands. The model spectrum of the ^{1,3}MLCT state is based on the high resolution $K\beta$ fluorescence spectra of $[Fe(bpy)_3]^{3+}$ and $[Fe(CN)_6]^{3-}$

presented in Figure S2B. The spectra of these compounds are very similar to each other. We have used the same weighing between $[Fe(bpy)_3]^{3+}$ and $[Fe(CN)_6]^{3-}$ for constructing the ^{1,3}MLCT reference as we derived for $[Fe(bpy)_3]^{2+}$ and $[Fe(CN)_6]^4$ in constructing the ground state reference. Using either $[Fe(bpy)_3]^{3+}$ or $[Fe(CN)_6]^{3-}$ alone as the ^{1,3}MLCT reference does not change the result of the following analysis.

Fig. S2. The ground-state and ^{1,3}MLCT reference spectra used in the analysis. (A) The ground state spectrum of $[Fe(CN)_4(bpy)]^{2-}$ recorded at the XFEL source (green circles), high-resolution ground state spectra of $[Fe(bpy)_3]^{2+}$ and $[Fe(CN)_6]^{4-}$ (red and blue) recorded at SSRL, and the linear combination of the $[Fe(bpy)_3]^{2+}$ and $[Fe(CN)_6]^{4-}$ spectra giving the best description of the $[Fe(CN)_4(bpy)]^{2-}$ spectrum (black). (B) High-resolution ground state spectra of $[Fe(bpy)_3]^{3+}$ and $[Fe(CN)_6]^{3-}$ (red and blue) recorded at SSRL, and the same linear combination of these spectra (black).
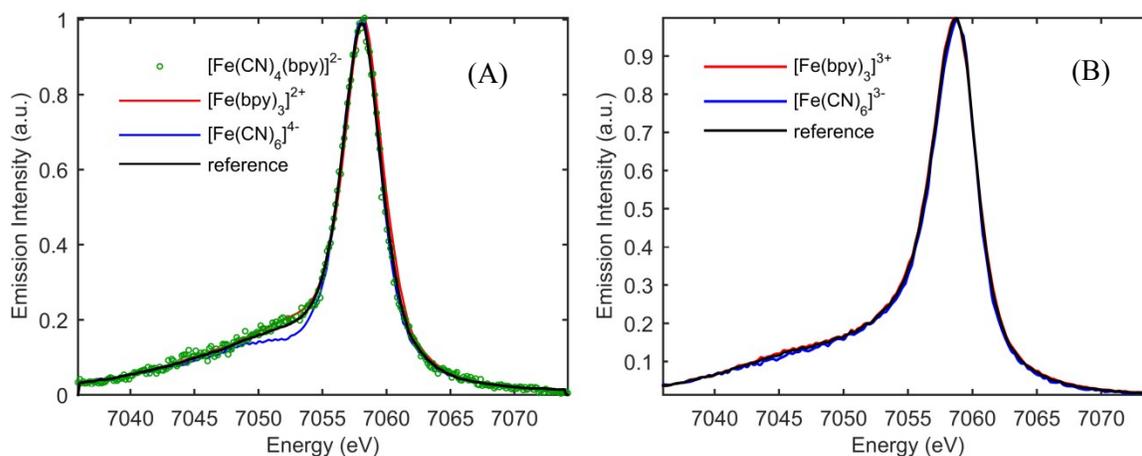
Fitting Transient Data

The transient Kβ spectrum of the 50 fs and 1 ps time delay is extracted from a time scan which was performed seven times. This allows for a straight-forward definition of the standard error of each data point as the standard deviation between the 7 repetitions divided by $\sqrt{7}$. The transient spectra from the main text is shown in Figure S3 with error bars representing the standard error, and the best fit to the data

using each of the four model reference difference spectra. While the differences between the reference spectra are relatively subtle, inspection of the Kβ' feature at 7045 eV, the shoulder at 7054 eV, and the zero-crossing at 7059 eV, shows that the ^{5}MLCT and ^{5}MC references are consistently outside the error bars of the measurement. Fitting the four reference difference spectra to the data, returns reduced chi-squared values of 1.4, 2.7, 4.6, and 9.8 for the ^{1,3}MLCT, ^{3}MC, ^{5}MLCT and ^{5}MC reference respectively. Using the formalism described in (Press 1986), the likelihood of a model describing a data set relates to the reduced chi-squared such that:

$$P \propto exp\boxed{?}\left(-\chi^2\right)$$

This relation makes it possible to quantitatively compare different fits (with the same number of free fit parameters) to a given dataset. Using the χ^2-values of the fits presented in Figure S3, the likelihood that the ^{3}MC, ^{5}MLCT and ^{5}MC references provides as good a description of the model underlying the recorded difference signal as the ^{1,3}MLCT reference is: 27%, 4%, and 0.02% respectively. This allows us to rule out the ^{5}MLCT and ^{5}MC states as dominant excited states with only the x-ray fluorescence measurement, but not the ^{3}MC. Only by joint consideration of the UV-visible and Kb fluorescence pump-probe measurements can the ^{3}MC excited state be ruled out.

Fig. S3. Kβ transient difference spectra for 50 mM $[Fe(CN)_4(bpy)]^{2-}$ in dimethyl sulfoxide obtained at 50 fs time delay (red circles) and 1 ps time delay (blue circles), fitted by the ^{1,3}MLCT (Fe $S = 1/2$) reference spectrum (black curve), ^{3}MC (Fe $S = 1$) reference spectrum (dashed black curve), ^{5}MLCT (Fe $S = 3/2$) reference spectrum (green curve), and the 5MC (Fe $S = 2$) reference spectrum (dashed green curve).
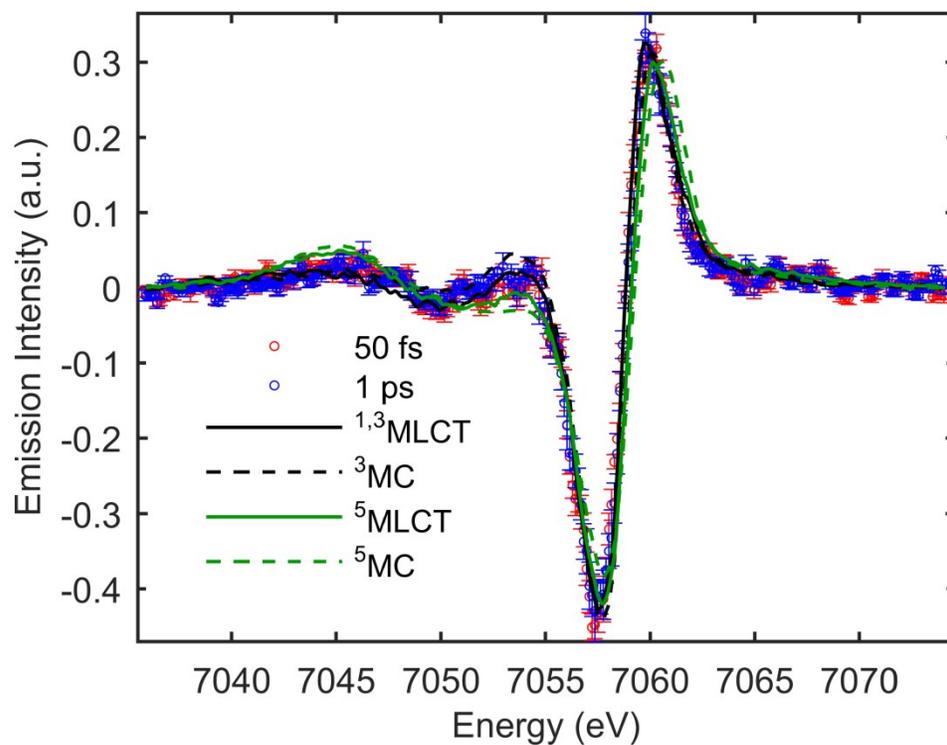
IV.   Computational Details

Full structural relaxations for all isolated metal complexes were performed using the Gaussian09 program,using the triple zeta basis set 6-311G(d,p), the PBE0 hybrid functional, and a PCM solvent description for DMSO. For each complex fully optimized geometries of the ground state (GS), ^{3}MLCT, ^{5}MLCT, ^{3}MC, and ^{5}MC excited states were found. Ground state properties have been calculated using the spin-restricted singlet formalism, while spin-unrestricted DFT (uDFT) calculations have been performed for the lowest triplet (^{3}MC, ^{3}MLCT) and quintet (^{5}MC, ^{5}MLCT) state calculations. Each calculated excited state can be assigned as MLCT or MC like based on its Fe spin density.

Table A. Calculated structural properties for each optimized minima using PBE0/6-311G(d,p)/PCM(DMSO).[a]

Geometry	E (eV)	Mulliken Spin on Fe	q_{bpy}[b]	q_{CN}[b]	R[c]	O[d]
GS	0	-	1.99 ± 0.001	1.92 ± 0.02	1.95 ± 0.04	1.98
^{3}MLCT	1.08	1.12	1.99	1.93 ± 0.01	1.95 ± 0.03	1.71
^{3}MC	0.84	2.07	2.25	2.01 ± 0.08	2.09 ± 0.14	3.58
^{5}MLCT	1.8	2.96	2.14 ± 0.00003	2.02 ± 0.08	2.06 ± 0.09	2.33
^{5}MC	0.86	3.83	2.27 ± 0.00004	2.20 ± 0.01	2.22 ± 0.04	4.77

[a] Distances in Å and angles in degrees; [b] q_{bpy} and q_{CN} are the composite reaction coordinates for bpy and CN ligands, respectively. They are calculated as the average of the Fe-C/N distances for each ligand; [c] R is the average of all metal coordinating atom bond distances; [d] average deviation $=(\sum|\text{ideal angle-measured angle}|)/n$;

Table B. Calculated energies for each spin state, singlet, triplet, and quintet, at each optimized geometry using PBE0/6-311G(d,p)/PCM(DMSO).

Geometry	S_O E (eV)	T_1 E (eV)	T_1 Mulliken Spin on Fe	Q_1 E (eV)	Q_1 Mulliken Spin on Fe
GS	0	1.28	1.11	2.69	2.83
^{3}MLCT	0.19	1.08	1.12	2.45	2.84
^{3}MC	0.8	0.84	2.07	2.07	2.98
^{5}MLCT	0.67	1.65	1.15	1.8	2.96
^{5}MC	1.70	1.51	2.04	0.86	3.83

Figure C. Triplet and quintet spin densities at each optimized geometry using PBE0/6-311G(d,p)/PCM(DMSO).

Geometry	T_1	Q_1
GS		
^{3}MLCT		
^{3}MC		
^{5}MLCT		
^{5}MC		
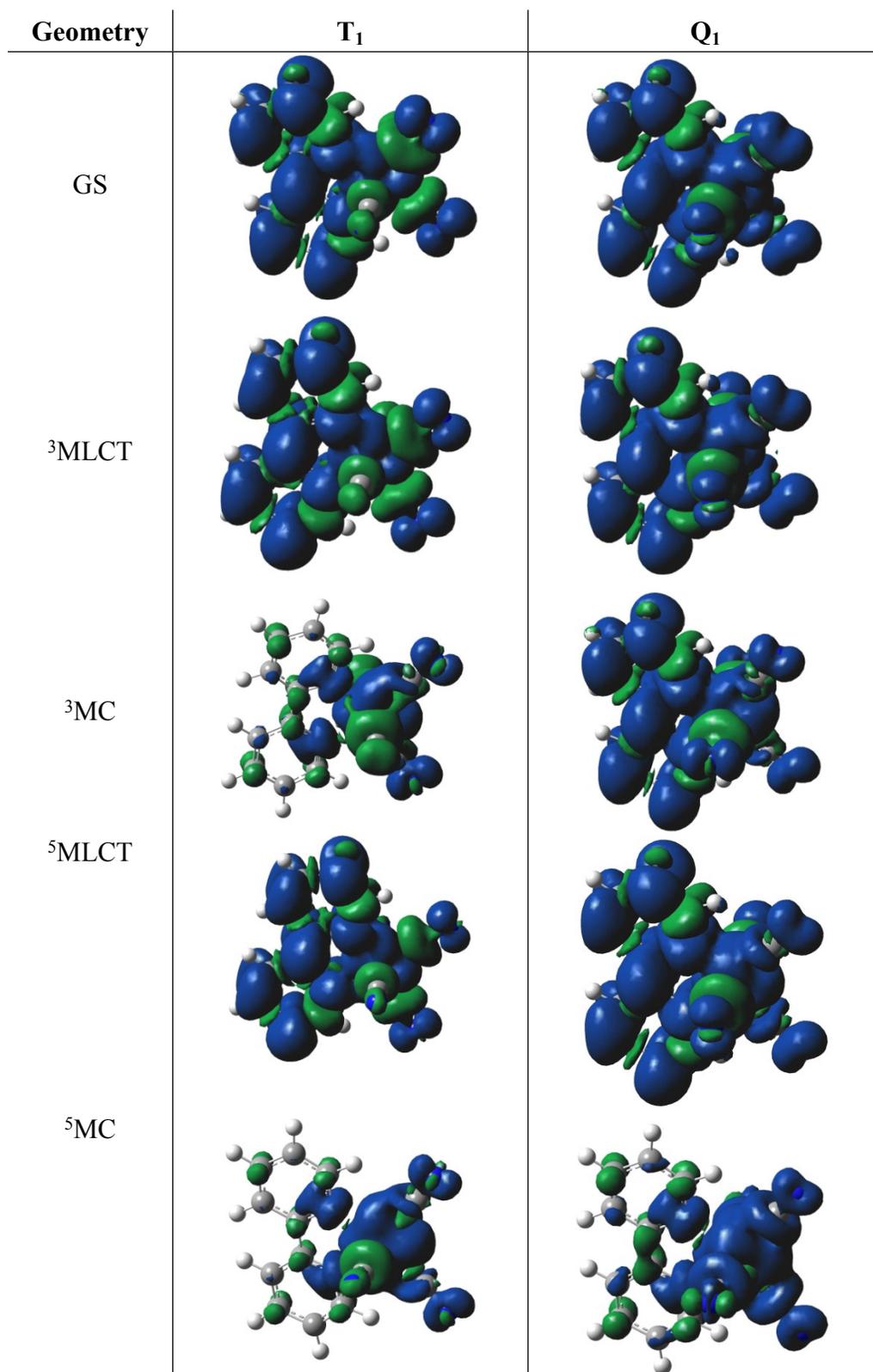
V.   References

(Henry) E.R. Henry and J. Hofrichter, *Methods in Enzyemology*, **210**, 129 (1992)

(Gawelda) W. Gawelda et al*., J. Am. Chem. Soc.* **129**, 8199 (2007).

(Winkler) J. R. Winkler, C. Creutz, and N. Sutin, *J. Am. Chem. Soc.* **109**, 3470 (1987)

(Horng) M. L. Horng, J. A. Gardecki, A. Papazyan, M. Maroncelli *J. Phys. Chem.,* **99**, 17311 (1995)

(Bhasikuttan) A. C. Bhasikuttan, M. Suzuki, S. Nakashima, T. Okada, *J. Am. Chem. Soc.* **124**, 8398 (2002)

(Zhang) W. Zhang et al. *Nature*, **509**, 345 (2014)

(Alonso-Mori 1) R. Alonso-Mori *et al.*, *Rev. Sci. Instrum.* **83**, 9 (2012).

(Koerner) L. J. Koerner, H. T. Philipp, M. S. Hromalik, M. W. Tate, S. M. Gruner, *J. Instrum.* **4**, 8 (2009).

(Alonso-Mori 2) R. Alonso-Mori et al., *Proc. Natl. Acad. Sci. U. S. A.* **109**, 19103 (2012).

(Harmand) M. Harmand et al., *Nature Photon.* **7**, 215 (2013).

(Vanko) Vanko, G.; Neisius, T.; Molnar, G.; Renz, F.; Karpati, S.; Shukla, A.; de Groot, F. M. F. J. Phys. Chem. B 2006, 110, 11647.

(Lee) Lee, N.; Petrenko, T.; Bergmann, U.; Neese, F.; DeBeer, S. J. Am. Chem. Soc. 2010, 132, 9715.

(Liu) Y. Liu *et al*., Chem Eur. J., 2015,21, 3628-3639.

(Pollock) Pollock, C. J.; Delgado-Jaime, M. U.; Atanasov, M.; Neese, F.; DeBeer, S. J. Am. Chem. Soc. 2014, 136, 9453.

(Press 1986) W. H. Press, B. P. Flannery, T. A. Teukolsky and W. T. Vetterling*, Numerical Recipes—The Art of Scientific Computing*, Cambridge University Press, Cambridge, 1986.